Inorganic Chemistry Communications 133 (2021) 108884

Contents lists available at ScienceDirect

Inorganic Chemistry Communications

journal homepage: www.elsevier.com/locate/inoche

Synthesis, structural determination, *Hirshfeld* surface analysis, 3D energy frameworks, electronic and (static, dynamic) NLO properties of *o*-Nitroacetanilide (*o*-NAA): A combined experimental and quantum chemical study

Nourdine Boukabcha [a,b], Amani Direm [c,*], Mokhtaria Drissi [a], Youcef Megrouss [a,b], Nawel Khelloul [a], Necmi Dege [d], Murat Tuna [e], Abdelkader Chouaih [a]

[a] Laboratory of Technology and Solid Properties (LTPS), Abdelhamid Ibn Badis University of Mostaganem, Mostaganem 27000, Algeria
[b] Chemistry Department, Faculty of Exact Sciences and Informatic, Hassiba Benbouali University, Chlef 02000, Algeria
[c] Laboratory of Structures, Properties and Interatomic Interactions LASPI2A, Department of Matter Sciences, Faculty of Sciences and Technology, Abbes Laghrour University, Khenchela 40.000, Algeria
[d] Department of Physics, Ondokuz Mayis University Samsun, Samsun 54187, Turkey
[e] Department of Chemistry, Faculty of Arts and Sciences, Sakarya University, Sakarya 54187, Turkey

ARTICLE INFO

Keywords:
NLO crystal
DFT
Electrostatic interactions
Hydrogen bonding
Energy framework

ABSTRACT

o-Nitroacetanilide (***o*-NAA**), an organic crystal, was synthesized and fully characterized by means of single-crystal XRD, FTIR, UV–visible, ^{1}H and ^{13}C NMR spectroscopic techniques. Its molecular structure was optimized, the subsequent electronic properties, the spectroscopic spectra were quantified using quantum chemical computations by density functional theory calculations and compared with the experimental results. Furthermore, the Mulliken atomic charges were estimated andthe molecular electrostatic potential map was plotted in order to identify the chemical reactive sites. To study the nonlinear optical (NLO) activity of ***o*-NAA**, the electric dipole moment, the static and dynamic polarizability and hyperpolarizabilities were computed indicating that it could be considered as a good candidate for NLO applications. The hydrogen bonding and the non-classical intermolecular interactions were investigated by performing a *Hirshfeld* surface analysis and their contributions were analyzed *via* the 2D-Fingerprint plots, thus revealing that the crystal structure of the studied molecule is mainly built up of H…H, H…O/O…H, H…C/C…H and C…O/O…C close contacts. From the 3D-molecular energy frameworks analysis, the *lattice energy* of the compound was found to be − 95.15 kJ.mol^{-1}, and has exhibited stabilizing strong C—H…O, N—H…C, *lp*…*lp*, *lp*…π and π…π interactions.

1. Introduction

Acetanilide derivatives are considered as an important class of materials in both chemistry and pharmaceutical industry owing to their large biological applications as analgesic as well as antipyretic agents [1] for the reason that they are mostly metabolized in the human body into paracetamol [2]. Furthermore, their applications are mainly related to thermodynamic properties [3],peculiar spectroscopy and quantum vibrational [4], herbicide properties [5] and their corrosion inhibition properties for 304L stainless steel [6]. An increasing interest of organic materials uses as nonlinear optical NLO devices has been noticed during the last years [7–8] due to their very large second-order electric susceptibilities [9] and their potential applications in electro-optic modulation [10,11], frequency conversion [12,13] and THz wave generation [14].Thus, nitroacetanilide derivatives, namely m- and p-substituted ones were investigated both experimentally and theoretically for their interesting NLO properties [15–17]. It is worth to be noted that a comprehensive and detailed structural literature survey of *o*-nitroacetanilide (***o*-NAA**) in the structural database (CSD, Version 5.39 [18]) revealed only the existence of one hit [19] reported in 1986, two hits for its derivatives 4-chloro-2-nitroacetanilide (CSD refcode : ICUMAU [20]) and4′-Fluoro-2′-nitroacetanilide (CSD refcode: NELQIE [21]), in addition to six more hits for the three 4-methyl-2-nitroacetanilide polymorphs appearing twice in the literature [22–23]. Moreover,

* Corresponding author.
E-mail addresses: amani_direm@yahoo.fr, direm.amani@univ-khenchela.dz (A. Direm).

https://doi.org/10.1016/j.inoche.2021.108884
Received 3 July 2021; Received in revised form 21 August 2021; Accepted 27 August 2021
Available online 1 September 2021

the database survey returned four other heterocyclic substitutes of ***o*-NAA**; namely 2-(3,5-Dimethyl-4-nitro-pyrazol-1-yl)-2′-nitroacetanilide, 2-(Pyrazol-1-yl)-2′-nitroacetanilide, 2-(3,5-Dimethylpyrazol-1-yl)-2′-nitroacetanilide and 2-(3,5-Dimethyl-4-iodo-pyrazol-1-yl)-2′-nitroacetanilide [24]. In order to contribute to the investigation of these systems, ***o*-NAA** was synthesized and fully characterized by means of single-crystal X-ray diffraction, FT-IR, NMR and UV–Vis spectroscopic techniques.

Since quantum chemical computational method using the density functional theory (DFT) is one of the reputed methods owing to its great accuracy in reproducing the experimental values of molecular geometry, spectroscopic parameters, atomic charges, dipole moment, thermodynamic properties, etc, DFT calculations were therefore adopted to optimize the structure of ***o*-NAA**. Additionally, in order to support the experimental results and to gain more insights into the molecular and physical properties of the studied molecule, HOMO and LUMO analysis, thermodynamic properties and Mulliken charges were calculated using both B3LYP/6 − 31G(d,p) and B3LYP/6 − 311G(d,p) basis sets. Furthermore, the ^{1}H and ^{13}C NMR chemical shifts of the molecule were computed using gauge including atomic orbital (GIAO) method and compared with the experimental results.

Moreover, the thermodynamic and the NLO properties as well as the electrostatic potential of the organic molecule, which contains expanded π-coupled electrons, were predicted and to the best of our knowledge will be reported for the first time. As no detailed quantitative investigation of the intermolecular interactions within the ***o*-NAA** crystal packing was previously reported, a comprehensive *Hirshfeld* surface and energy frameworks analyses of the molecule's contacts was performed and its intermolecular interactions were therefore fully discussed in terms of their energies.

2. Materials and methods

2.1. Synthesis of o-NAA

o-Nitroaniline (0.02 mol) was dissolved in acetic anhydride (0.02 mol) at room temperature as indicated by the chemical pathways in Scheme 1. After one hour, a yellow-colored solid was obtained which was then filtered, dried using vacuum filtration and recrystallized in methanol. Single crystals of *o*-nitroacetanilide (***o*-NAA**) were grown after slow evaporation at room temperature.

2.2. Spectroscopic measurements

Electronic spectrum of ***o*-NAA** was measured on a Shimadzu UV-2600 Pc-spectrophotometer with quartz cell of 1 cm. Infrared spectrum was recorded on a Perkin Elmer Spectrum Two FT-IR spectrophotometer equipped with Perkin Elmer UATR-TWO diamond ATR and corrected by applying the ATR correction function of Perkin Elmer Spectrum software. Its ^{1}H and ^{13}C NMR spectra were obtained using $CDCl_3$ and DMSO-d_6 solutions on a Varian Mercury Plus 300 MHz spectrometer.

2.3. Single-crystal X-ray data collection and structure refinement

Single-crystal X-ray diffraction data of the studied molecule were collected on a STOE IPDS II. All diffraction measurements were performed at 298 K using monochromated MoKα radiation (λ = 0.71073 Å). X-AREA and X-Red32 programs [25] were used ford ata reduction and cell refinement, respectively. ShelxS [26] and ShelxL [27] programs were used to solve and refine the structure, respectively. The structure was determined by considering 1483 reflections with $I > 2\sigma(I)$. All non-H atoms were anisotropically refined, while H atoms were obtained from the difference Fourier maps and refined using a riding mode on their parent atoms with C–H = 0.930 Å and $U_{iso}(H) = 1.2U_{eq}(C)$. The crystal structure validations and geometrical calculations were performed using Platon [28] and Mercury software [29]. The details of the crystallographic parameters, data collection and refinement are given in Table 1. Furthermore, the asymmetric unit of the reported molecule is illustrated in Fig. 1.a.

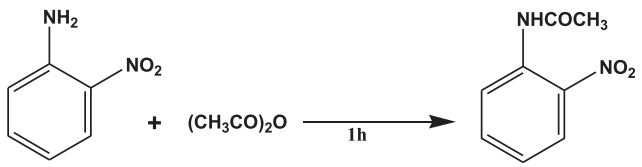

Scheme 1. Synthesis of *o*-nitroacetanilide (***o*-NAA**).

2.4. Computational details

The ground state calculations were performed using the Gaussian 09 set of quantum chemistry codes [30]. The output files were visualized *via* Gauss View 5 software [31]. The structural properties of ***o*-NAA** were determined by applying Becke's three-parameter hybrid functional (B3) for the exchange part and the Lee-Yang-Parr (LYP) correlation function [32] with 6-31G(d,p) and 6-311G(d,p) levels in order to obtain the optimized geometrical parameters, the vibrational wavenumbers of the normal modes, the IR intensities and thermodynamic parameters of the compound. The complete assignments were performed on the basis of the Potential Energy Distribution (PED) of the vibrational modes calculated using vibrational Energy Distribution Analysis (VEDA) 4 program [33]. The MEP and HOMO–LUMO energies were calculated at the same level. Additionally, the dipole moment (μ), the mean polarizability (α), the first-order static hyperpolrizability (β) and the second-order static hyperpolrizability (γ) were all computed in order to evaluate the NLO properties of ***o*-NAA**. The dynamic first- and second hyperpolarizabilities were also evaluated theoretically. Furthermore, in order to get detailed insights into the different intermolecular interactions in the crystal packing of ***o*-NAA**, a complete *Hirshfeld* surface analysis together with an energy frameworks analysis were performed using CrystalExplorer17.5 program [34].

Table 1
Crystal data and refinement parameters of ***o*-NAA**.

Compound	***o*-NAA**
Empirical formula	$C_8H_8N_2O_3$
Formula weight (M_r)	180
Temperature (K)	298
Wavelengh (Å)	0.71073
Crystal	Monoclinic
Space group	$P2_1/n$
A	10.9245(19)
B	4.9658(6)
C	15.545(2)
B	97.877(13)
V (Å^3)	803.4(2)
Z	4
Radiation type	Mo $K\alpha$
Density (g cm-3)	1.433
μ (mm^{-1})	0.77
F(000)	376
θ range for data correction	24.996
R_{int}	0.0484
h, k, l	$-13 \le h \le 13$, $-6 \le k \le 6$, $-19 \le l \le 20$
Number of measured, independent and observed [$I > 2\sigma(I)$] reflections	11870, 1844, 1483
$R[F^2 > 2\sigma(F^2)]$ / $wR(F^2)$ / S	0.0416 / 0.0556 / 1.03
Number of parameters	123
$\Delta\rho_{max}$ / $\Delta\rho_{min}$ (e Å^{-3})	0.71 / −0.31
Goodness of fit F^2 (S)	1.03
R indices [I > 2σ(I)]	$R_1 = 0.0416$. $wR_2 = 0.111$

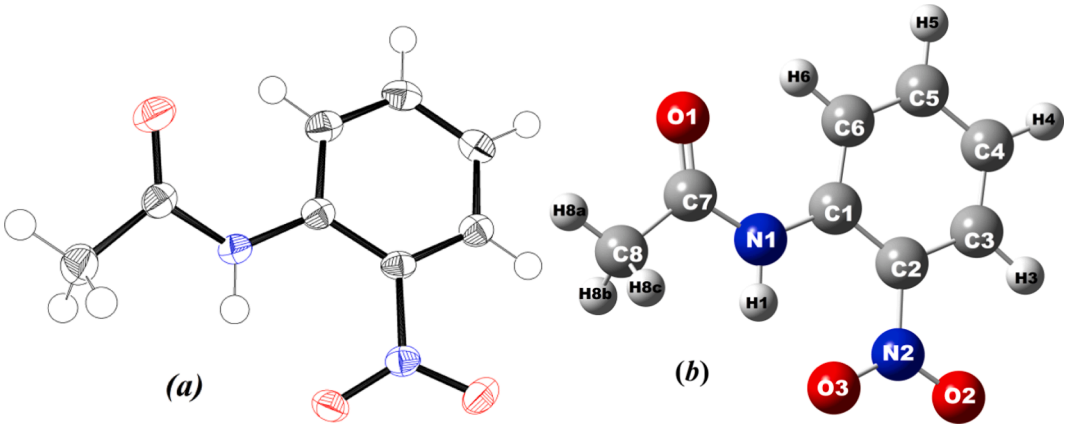

Fig. 1. (a) Asymmetric unit, ellipsoids drawn at 50%, and (b) optimized structure of ***o*-NAA**.

3. Results and discussion

3.1. Molecular geometry

The optimized geometrical parameters of ***o*-NAA** are listed in Table 2. Its optimized molecular structure is shown in Fig. 1.b. From Table 2, it can be seen that the computed bond lengths and angles show a good agreement with the experimental X-ray diffraction results. The mean C—C bond length value within the ring is found to be ≈ 1.398 Å at DFT/B3LYP method with both 6-31G(d,p) and 6-311G(d,p) basis sets, and agree well with the mean experimental value equal to 1.393 Å. The bond lengths were calculated in the range 1.222–1.516 Å for 6-31G(d,p) and 1.220–1.518 Å for the 6-311G(d,p) basis set. Whereas, the optimized angles were found to vary from 112.65° to 129.02° for B3LYP/6-31G(d,p) and from 113.05° to 129.09° for B3LYP/6-311G(d,p).Thus, the bond lengths show a maximum deviation of 0.016 Å and 0.172 Å observed for the C7—C8 and C7—O1 bonds estimated using B3LYP/6-31G(d,p) and B3LYP/6-311G(d,p), respectively. Whereas, it is found that the maximum deviation value of the bond angles is 1.82° and 1.89°, obtained by the B3LYP/6-31G(d,p) and B3LYP/6-311G(d,p) basis sets. These values are associated to the C1—N1—C7 angle and are not quite significant.

Table 2
Selected experimental and theoretical bond lengths and angles within ***o*-NAA**.

			Experimental	B3LYP/6-31G(d,p)	B3LYP/6-311G(d,p)
Bond lengths (Å)					
C1	C2		1.414	1.421	1.422
C2	C3		1.389	1.401	1.398
C1	C6		1.405	1.412	1.409
C3	C4		1.379	1.381	1.380
C4	C5		1.391	1.395	1.397
C5	C6		1.382	1.383	1.384
C7	C8		1.500	1.516	1.518
C7	O1		1.217	1.222	1.229
N2	O2		1.234	1.231	1.220
N2	O3		1.229	1.240	1.239
N1	C1		1.394	1.387	1.389
N1	C7		1.379	1.386	1.389
N2	C2		1.464	1.466	1.469
Bond angles (°)					
C1	N1	C7	127.2	129.02	129.09
O2	N2	O3	122.5	122.12	122.54
O2	N2	C2	119.6	118.47	118.42
O3	N2	C2	117.83	119.39	119.03
N1	C1	C2	121.9	121.11	121.33
N1	C1	C6	121.6	121.95	121.86
C2	C1	C6	116.3	116.93	116.79
C1	C2	C3	122.1	121.21	121.25
N2	C2	C1	121.6	123.05	123.05
N2	C2	C3	116.2	115.73	115.69
C2	C3	C4	120.0	120.52	120.58
C3	C4	C5	119.1	118.93	118.89
C4	C5	C6	121.1	121.36	121.34
C1	C6	C5	121.2	121.02	121.11
O1	C7	N1	123.8	124.57	124.62
O1	C7	C8	123.0	122.68	122.79
N1	C7	C8	113.1	112.65	113.05

3.2. Vibrational band assignments

The vibrational spectral assignments of the recorded FT-IR spectra of ***o*-NAA** (Fig. 2) were performed based on the theoretical predicted wavenumbers using the 6 − 31G(d,p) and 6 − 311G(d,p) basis set as shown in Table 3. The studied molecule consists of 21 atoms, which undergo 57 (3 N-6) normal modes of vibrations, where N is the number of atoms. The detailed vibrational assignments of the experimental wavenumbers were based on normal mode analysis and compared with the theoretically scaled wavenumbers.

None of the predicted vibrational bands of ***o*-NAA** have an imaginary frequency, implying that the optimized geometry is located at the local lowest point on the potential energy surface. The DFT levels overestimate the vibrational wavenumbers due to the well-known systematic errors. Thus, the scaling factor of 0.9614 was used to calibrate the calculated vibration frequencies. The detailed assignments of the vibration modes were provided by means of the potential energy distribution (PED) analysis. The detailed assignments of the vibration frequencies for ***o*-NAA** were presented in Table 3, by providing combined experimental and theoretical results.

The N—H stretching vibration should occur in the region 3450–3250

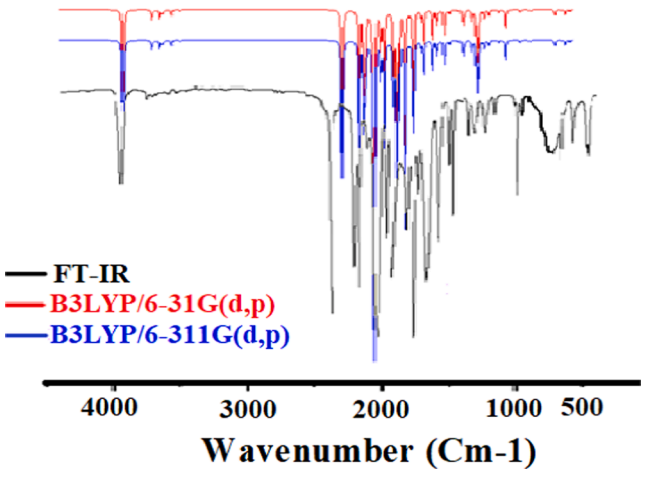

Fig. 2. Experimental and theoretical IR spectra of ***o*-NAA**.

Table 3
Measured and calculated frequencies (cm^{-1}), IR intensity (km/mol) and probable assignments characterized by PED of the molecule ***o*-NAA**.

FT-IR	B3LYP/6-31G(d,p)		B3LYP/6-311G(dp)		Assignments with PED > 10%
	Scaled freq.	I_{IR}	Scaled freq	I_{IR}	
3369	3492	150.97	3353.28	150.93	υ NH (99)
	3270	12.51	3139.2	12.51	υ CH (99)
	3252	2.97	3121.92	2.97	υ CH (96)
	3216	10.02	3087.36	10.02	υ CH (81) + υ CH (16)
	3119	7.23	2994.24	7.23	υ CH asym (50) + υ CH sym (50)
	3054	2.43	2931.84	2.39	υ CH3 (1 0 0)
1717	1798	165.5	1726.08	170.23	υ OC (82)
1611	1601	115.7	1604.16	116.04	υ ON asym (11) + υ CC sym (11) + υ ON (21)
1588	1577	151.10	1571.52	150.01	υ CC asym (16) + δHNC (24) + δCCC asym(13)
	1560	87.44	1556.16	86.54	υ ON (19) + υ CC sym (15) + υ ON (16)
1501	1494	8.46	1492.8	605.15	υ CC sym (10) + υ NC (11) + δHNC 17) + δHNC asym (11)
1456	1435	6.72	1434.24	8.46	δHCH asym (37) + δHCH sym (37) + τ HCCNasym (20)
1432	1403	9.3	1424.64	7.47	δHCH asym (31) + δHCH sym (22)
1367	1359	80.65	1346.88	96.31	δHCH sym (79)
1338	1311	206.74	1325.76	241.01	υ ON (39) + υ NC (10)
1316	1300	75.78	1304.64	80.65	υ CC sym (29) + υ CC asym (29)
1277	1250	122.64	1258.56	206.74	υ ON asym (14) + υ CC asym (13) + υ NC (17) + δHCC (26)
1163	1190	8.11	1200	122.64	υ NC (28) + υ CC asym (13) + δHNC (13) + δOCC (12)
1082	1103	33.84	1123.2	52.90	υ CC sym (29) + δHCC asym (25) + δHCC (18)
1045	1010	35.68	1010.88	5.04	δHCH (10) + δHCH asym (10) + τ HCCNasym(13) + τ HCCN(26) + τ HCCN asym (13) + γOCNC(10)
958	982	1.72	969.6	1.46	δHCH (11) + τ HCCN(22) + τ HCCNasym(23)
899	865	22.45	866.88	2.12	τ HCCCasym(35) + τ HCCCsym(55)
	797	16.57	814.08	1.79	υ CC (18) + υ NC (11) + δONO (10) + δCCC (12).
	766	29.40	765.12	16.57	τ HCCC(63) + γOCON(20)
651	666	9.07	677.76		τ CCCC(35) + γOCON asym (25) + γNCCC(22)
593	640	8.23	639.36	7.21	υ CC (11) + βCCCasym(12) + δOCC(10) + δCCC(32)
531	535	13.38	539.52	9.07	υ CC (10) + δOCC(10) + δONCasym(13) + δCCCasym(13) + δCCCasym(15) + δNCC(18)
	422	2.97	405.12	8.54	υ NC (35) + δCCC(12) + δCCN(11)+

ν: stretching ; sym: symmetric ; asym: asymmetric; β: in plane bending ; γ: out–of plane bending ; τ : twisting ; δ: bending. Vibrational modes are based on the potential energy distribution (PED) and only contributions over 10% are given. Scaled frequencies are in the unit cm^{-1} and I_{IR} infrared intern are in $km.mol^{-1}$.

cm^{-1} [35] and is observed to be at 3369 cm^{-1} in the experimental spectrum (Fig. 2). On the other hand, the corresponding values calculated with the B3LYP/6-31G(d,p) and B3LYP/6-311G(d,p) methods were found to be respectively 3492 and 3353.28 cm^{-1}, based on the results of the PED analysis shown in Table 3.

Aromatic structures show the presence of C—H stretching vibrations in the characteristic region 3100–3000 cm^{-1} [36–38] and the experimental band is hence found to share with the N—H stretching mode the wavenumber 3369 cm^{-1}. The computed wave numbers at 3139.2, 3121.9 and 3087.3 cm^{-1} obtained from the B3LYP/6-311G(d,p) method correspond to the C—H symmetric stretching vibrations with PED values of 99%, 96% and 81%, respectively. It is worth to be noted that both the C—H symmetric and asymmetric stretching bands are computed at 2994.2 $cm^{-1}$with a PED of 50%. The corresponding values obtained from the B3LYP/6-31G(d,p) method are respectively 3270, 3252, 3216 and 3119 cm^{-1} with the same PED values.

From the previously reported C═O stretching frequencies [35,39], the wavenumbers appear within the range 1850–1600 cm^{-1}. In this study, the experimental C═O vibration is observed at 1717 cm^{-1}. Moreover, the calculated wavenumbers by the B3LYP/6-31G(d,p) and B3LYP/6-311G(d,p) methods being at 1798 and 1726 cm^{-1} are well consistent with the experimental values, as shown in Table 3.

Whereas, the asymmetric stretching bands in $–NO_2$-containing molecules are expected to appear in the region 1625–1540 cm^{-1} and the symmetric ones in the region 1400–1360 cm^{-1} [40–43]. The asymmetric stretching mode of the N—O bonds is calculated *via* B3LYP/6-31G(d,p) and B3LYP/6-311G(d,p) methods with a PED value of 11 % at 1601 and 1604.1 cm^{-1}, respectively. However, the N—O symmetric stretching vibration was computed to be 1560 and 1556.1 cm^{-1} with a PED of 19%. Thus, the experimental band appearing at 1622 $cm^{-1}$is attributed to these corresponding N—O vibrations. The nitro group is additionally capable of different bending vibrations such as scissoring, wagging, rocking and twisting. All these vibrations give rise to several variable intensity bands at lower wavenumbers.

Additionally, the C—N stretching band should appear in the region 1260–1380 cm^{-1}. In the experimental spectrum of ***o*-NAA**, these vibration modes occur within 1163–1338 cm^{-1}, whereas the associated B3LYP/6-31G(d,p) and B3LYP/6-311G(d,p) calculated values are in the region 1190–1311 and 1200–1325.7 cm^{-1}.

3.3. *^{1}H and ^{13}CNMR spectra analysis*

The ^{1}H and ^{13}C NMR chemical shifts of ***o*-NAA** are calculated using the gage-including atomic orbital (GIAO) method by applying the B3LYP/6-31G(d,p) and B3LYP/6-311G(d,p) levels. Their values were obtained by subtracting isotropic magnetic shielding (IMS) values, which are calculated with GIAO, from the IMS values of TMS [44–47]. Hence, a comparison of the corresponding experimental and theoretical chemical shifts in ppm useful to perform correct assignments in the spectra of ***o*-NAA** is given in Table 4. The computed ^{13}C NMR chemical shift values are ranging from 17.5 to 154.09 ppm for B3LYP/6-31G(d,p) and from 27.3 to 172.15 for the B3LYP/6-311G(d,p) level. Whereas, the measured ones are found to be in the range 25.46–169.19 ppm.

Table 4
The experimental and calculated ^{1}H and ^{13}C NMR chemical shifts of ***o*-NAA**.

Chemical shifts (ppm)			
	Experimental	B3LYP/6–31G(d,p)	B3LYP/6–311G(d,p)
^{1}HNMR			
H3	8.76	8.76	8.56
H4	7.65	7.29	7.68
H5	7.65	7.83	7.09
H6	8.20	9.89	9.62
H1	10.3	11.97	11.49
H8A	2.29	2.00	1.85
H8B	2.29	2.56	2.35
H8C	2.29	2.56	2.35
^{13}CNMR			
C1	134.75	127.51	145.46
C2	136.52	122.76	141.33
C3	125.63	115.04	131.98
C4	123.25	108.54	125.70
C5	135.81	124.43	143.06
C6	122.25	109.14	125.70
C7	169.19	154.09	172.15
C8	25.46	17.50	27.30

Additionally, the computed ^{1}H NMR chemical shifts, varying from 2.00 to 11.97 ppm and from 1.85 to 11.49 ppm using respectively the B3LYP/6-31G(d,p) and the B3LYP/6-311G(d,p) levels, are comparable with the experimental ones being in the range 2.29–10.3 ppm, as it can be seen from Table 4. Therefore, the overall computed and measured ^{1}H and ^{13}C NMR chemical shift of ***o*-NAA** are in agreement except for the C4 atom.

3.4. UV–Visible spectral analysis

The UV–Visible spectrum of ***o*-NAA** was calculated by means of TD-B3LYP/6-31G(d,p) and TD-B3LYP/6-311G(d,p) methods and compared along with the measured UV–Visible data (Table 5 and Fig. 3). The absorption maxima for the low laying singlet states of ***o*-NAA**, which are functions of electron availability calculated by both methods, appear at 370, 274 and 250 nm for both levels. As concluded from Table 5, the maximum absorption wavelength corresponding to the contribution of HOMO → LUMO (+97%), HOMO-2 → LUMO (92%), HOMO → LUMO + 1 (5%), HOMO-3 → LUMO (53%), HOMO-1 → LUMO (41%) and HOMO-5 → LUMO (3%) are associated to the n → π* electronic transition.

3.5. Mulliken atomic charges

The calculated Mulliken atomic charges of the studied compound are presented in Table 6. The obtained values show that the C3, C4, C5, C6, C8, O1, O2, O3 and N1 atoms have larger negative atomic charges. While those of the C1, C2, C7 and N2 atoms are largely positive. The charge of the H1 atom has the maximum magnitude of 0.3073 among the remaining hydrogen atoms present in the molecule at both the B3LYP/6 − 31G(d,p) and B3LYP/6 − 311G(d,p) theoretical levels. However, all the hydrogen atoms exhibit net positive charges and their magnitudes are varying between [0.1028–0.3073] for B3LYP/6 − 31G (d,p) and between [0.1063–0.2646] for the B3LYP/6 − 311G(d,p) level. It is worth to be noted that in the ***o*-NAA** molecule, the C8 atom has a highest negative value.

3.6. Frontier molecular orbitals analysis

Named as frontier molecular orbital (FMOs), both the highest occupied molecular orbital (HOMO) is an electron donor and the lowest unoccupied molecular orbital (LUMO) is an electron acceptor one. In the present study, the HOMO and LUMO energies were predicted at B3LYP method with the 6-31G(d,p) and 6-311G(d,p) basis sets. According to the obtained results, the energy gap between the HOMOs and LUMOs represents the critical parameter in determining the molecular electrical transport properties which help the electron conductivity measurement. The distributions and energy levels of (HOMO → LUMO), (HOMO-1 → LUMO + 1) and (HOMO-2 → LUMO + 2) orbitals of the studied molecule are shown in Fig. 4, in order to understand its bonding feature. Thus, their frontier molecular gap values were found to be 4.06, 6.55 and 7.69 eV respectively. This electronic absorption corresponds to the transition from the ground to the first excited state and is mainly described by one electron excitation from HOMO to LUMO. The HOMO is located over the NH and NO_2 group, while the LUMO is located over the nitrobenzene.

Table 5
Experimental and theoretical electronic transitions, oscillator strength and major contributions for ***o*-NAA**.

Experimental	Theoretical				
λ = 342 nm	λ (nm)	Osc. strength	Major contributions with B3LYP/6-311G(d,p)		
	370	0.0888	HOMO → LUMO (97%)	.	
	274	0.1494	HOMO −2 → LUMO (92%)	HOMO → LUMO + 1 (5%)	
	250	0.0500	HOMO −3 → LUMO (53%)	HOMO −1 → LUMO (41%)	HOMO-5 → LUMO (3%)
	λ (nm)	Osc. strength	Major contributions with B3LYP/6-31G(d,p)		
	370	0.0882	HOMO → LUMO (97%)		
	272	0.1502	HOMO −2 → LUMO (92%)	HOMO → LUMO + 1 (5%)	
	249	0.135	HOMO −3 → LUMO (58%)	HOMO −1 → LUMO (36%)	

The frontier molecular orbitals' energies (E_{HOMO}, E_{LUMO}) were used to calculate the global chemical reactivity descriptors of the molecule such as the ionization potential electron affinity, the electronegativity, the global hardness, the global softness, the chemical potential and the electrophilicity index [48–53]. These important descriptors are calculated as follows:

$$Ionizationpotential : I_P = -E_{HOMO}$$

$$Electronaffinity : E_A = -E_{LUMO}$$

$$\text{Electronegativity} : \chi = -\frac{1}{2}(E_{LUMO} + E_{HOMO})$$

$$\text{Chemicalpotential} : P = 1/2(E_{LUMO} + E_{HOMO})$$

$$\text{Globalhardness} : \eta = 1/2(E_{LUMO} - E_{HOMO})$$

$$\text{Globalsoftness} : S = 1/2\eta$$

$$\text{Electrophilicityindex} : \omega = \frac{\mu^2}{2\eta}$$

Where A is the ionization potential and I is the electron affinity of the molecule. Both parameters can be expressed through HOMO and LUMO orbital energies as $I = -E_{HOMO}$ and $E_A = -E_{LUMO}$. The electroaffinity and the Ionization potential of ***o*-NAA** are given in Table 7. The calculated values of the softness, the hardness, the chemical potential, the electronegativity and the electrophilicity index of the molecule are found to be respectively 1.02, 2.03, –4.97, 4.97 and 6.08 eV by B3LYP/6-311G(d,p) and 1.01, 2.01, –4.75, 4.75 and 5.61 eV by B3LYP/6-31G(d,p). The soft molecule represents a small HOMO-LUMO gap, while that of the hard molecule is supposed to be large.

3.7. Nonlinear optical properties

Nonlinear optical (NLO) effects arise from the interactions of the electromagnetic fields in various media to produce new fields altered in phase, frequency amplitude or other propagation characteristics from the incident fields [54]. The NLO property is at the forefront of current research because of its importance in providing the key functions of frequency shifting, optical logic and optical memory for the emerging technologies such as telecommunications, signal processing and optical interconnections [55–58]. To investigate the NLO behavior of ***o*-NAA**, the electric dipole moment, the polarizability and the first and second order hyperpolarizabilities were calculated using the DFT/B3LYP method with 6-31G(d,p) and 6-311G(d,p) basis sets. The polarizability and hyperpolarizability tensors (α_{xx}, α_{xy}, α_{yy}, α_{xz}, α_{yz}, α_{zz}, and β_{xxx}, β_{xxy}, β_{xyy}, β_{yyy}, β_{xxz}, β_{xyz}, β_{yyz}, β_{xzz}, β_{yzz}, β_{zzz}, and γ_{xxxx}, γ_{yyyy}, γ_{zzzz}, γ_{xxyy}, γ_{xxzz}, γ_{yyzz}) can be obtained by a frequency job output file of Gaussian 09. The total dipole moment, the mean polarizability (α_{tot}) and the first order hyperpolarizability ($\beta_{||}$) can be calculated using the following equation [59]:

$$\mu = (\mu_x^2 + \mu_y^2 + \mu_Z^2)^{\frac{1}{2}}; \alpha = \frac{1}{3}(\alpha_{xx} + \alpha_{yy} + \alpha_{zz}); \beta\| = (\beta_x^2 + \beta_y^2 + \beta_z^2)^{\frac{1}{2}}$$

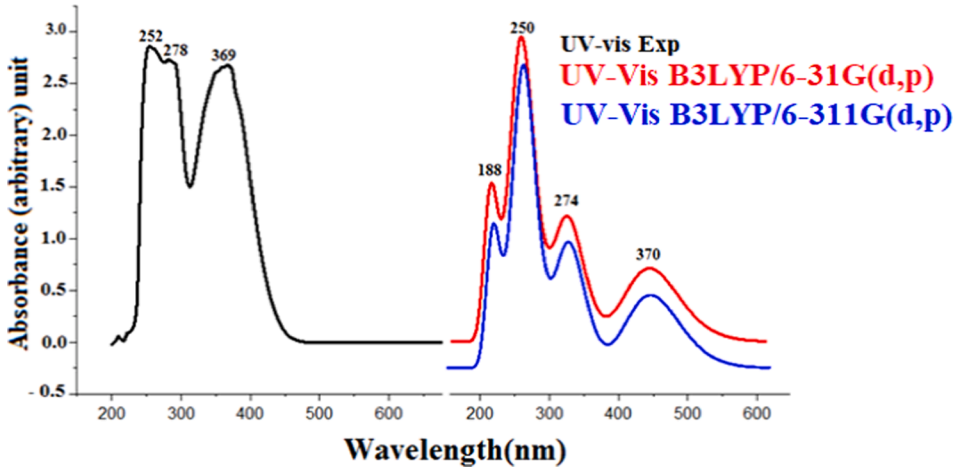

Fig. 3. Experimental and theoretical UV–Visible spectra of ***o*-NAA.**

Table 6
Mulliken atomic charges within ***o*-NAA.**

Atoms	DFT/B3LYP	
	6–31G(d,p)	6–311G(d,p)
C1	0.3199	0.2161
C2	0.2288	0.1331
C3	−0.1036	−0.0696
C4	−0.0938	−0.0891
C5	−0.0829	−0.0725
C6	−0.1073	−0.0977
C7	0.5716	0.3285
C8	−0.4077	−0.3349
N1	−0.6403	−0.4550
N2	0.3767	0.1780
O1	−0.4768	−0.3457
O2	−0.4422	−0.3259
O3	−0.3888	−0.2566
H3	0.1419	0.1392
H4	0.1028	0.1063
H5	0.1075	0.1105
H6	0.1542	0.1521
H1	0.3073	0.2646
H8A	0.1412	0.1372
H8B	0.1502	0.1445
H8C	0.1412	0.1372

The complete equation for calculating the magnitude of the first order hyperpolarizability is given as follows:

$$\beta\| = \left[\left(\beta_{xxx}+\beta_{xyy}+\beta_{xzz}\right)^2+\left(\beta_{yyy}+\beta_{yzz}+\beta_{yxx}\right)^2+\left(\beta_{zzz}+\beta_{zxx}+\beta_{zyy}\right)^2\right]^{\frac{1}{2}}$$

The average (or absolute value) of static second-order hyperpolarizability can be simplified *via* the Kleinmann [60] approach and computed through the expression:

$$\gamma = \frac{1}{5}\left(\gamma_{xxxx}+\gamma_{yyyy}+\gamma_{zzzz}+2\gamma_{xxyy}+2\gamma_{xxzz}+2\gamma_{yyzz}\right)$$

The calculated dipole moment (μ), isotropic polarizability (α), static first order hyperpolarizability ($\beta_{||}$) and the static second order hyperpolarizability (γ) for ***o*-NAA** are listed in Table 8. It is well known that the higher the values of the dipole moment, the molecular polarizability and the hyperpolarizabilities, the more active NLO properties will be. Moreover, the polarizability and the hyperpolarizabilities are reported in the atomic units (a.u) (for α 1 au = 0.1482×10^{-24} esu, for β 1 au = $8.63922\ 10^{-33}$ esu and for γ 1 au = $5.03670\ 10^{-40}$ esu). The values of the dipole moment obtained respectively from B3LYP/6-31G(d,p) and B3LYP/6-311G(d,p) are equal to 1.29309 and 1.32949 D, which are similar to the values reported in the literature for organic molecules [61,62]. The highest value of the dipole moment is observed for μ_z component. Furthermore, the calculated polarizability values of ***o*-NAA** are found to be 16.397×10^{-24} esu for B3LYP/6-31G(d,p) and 17.221×10^{-24} esu for B3LYP/6-311G(d,p). For this parameter, the highest value is obtained for α_{xx} component with 159.613 au which means that there is a considerable delocalization in this direction. The magnitude of the molecular hyperpolarizability β is one of important key factors in an NLO molecular system. Thus, the first hyperpolarizability (β) values of ***o*-NAA** calculated at B3LYP/6-31G(d,p) and B3LYP/6-311G(d,p) levels are equal to 2.312×10^{-30} esu and 2.226×10^{-30} esu, respectively. Similarly, the computed second-order hyperpolarizability (γ) values for the ***o*-NAA** molecule using 6-31G(d,p) and 6-311G(d,p) basis sets along with the B3LYP functional are 5.82 and 7.42×10^{-36} esu, respectively. Based on the above results, the ***o*-NAA** molecule could be considered as one of the typical molecules for optoelectronic and NLO applications.

For a molecular system, the NLO properties can be determined by their dynamic hyperpolarizabilities. In this work, dynamic parameters of ***o*-NAA** were calculated using B3LYP functional with the two basis sets 6-31G(d,p) and 6-311G(d,p) at λ = 1139.1 and λ = 911.3 nm, respectively. These results are presented for α(−ω;ω) and $\beta_{||}z(-\omega;\omega,0)$ corresponding to the Pockels electro-optic effect, and $\beta_{||}z(-2\omega;\omega,\omega)$ associated to the second harmonic generation (SHG). The dynamic hyperpolarizabilities γ(−ω;ω,0,0) and γ(−2ω;ω,ω,0) are related to the quadratic electro-optical Kerr effect (dc-Kerr effect) and dc-SHG. The dynamic polarizability α(−ω;ω) values are 16.6905 and 17.7293×10^{-24} esu calculated at B3LYP/6-31G** and B3LYP/6-311G** levels, respectively. The dynamic hyperpolarizabilities related to the electro-optical Pockels effect, $\beta_{||}z(-\omega;\omega,0)$ and the second harmonic generation, $\beta_{||}z(-2\omega;\omega,\omega)$ were predicted and the corresponding values are close to zero reflecting the centrosymmetry of the medium. The predicted values for $\beta_{||}z(-\omega;\omega,0)$ and $\beta_{||}z(-2\omega;\omega,\omega)$ are 0.000033 and 0.000187×10^{-30} esu obtained at B3LYP/6-31G** level, and − 2.78597 and − 7.07814×10^{-30} esu obtained at B3LYP/6-311G** level, respectively. The calculated values of the frequency dependent second hyperpolarizability for the dc-Kerr effect, γ(−ω;ω,0,0) and the electric-field induced second harmonic generation, γ(−2ω;ω,ω,0) are 6.76974 and 10.2631×10^{-36} esu obtained at B3LYP/6-31G** level, and 9.29214 and 23.0055×10^{-36} esu obtained at B3LYP/6-311G** level, respectively. The second-order hyperpolarizability values correspond well to the previously published results [63]. In addition to the above discussion, the title molecule exhibits a huge third-order nonlinearity.

3.8. Molecular electrostatic potential

The molecular electrostatic potential (MEP) is basically a three dimensional plot for the total electron density which is used to analyze

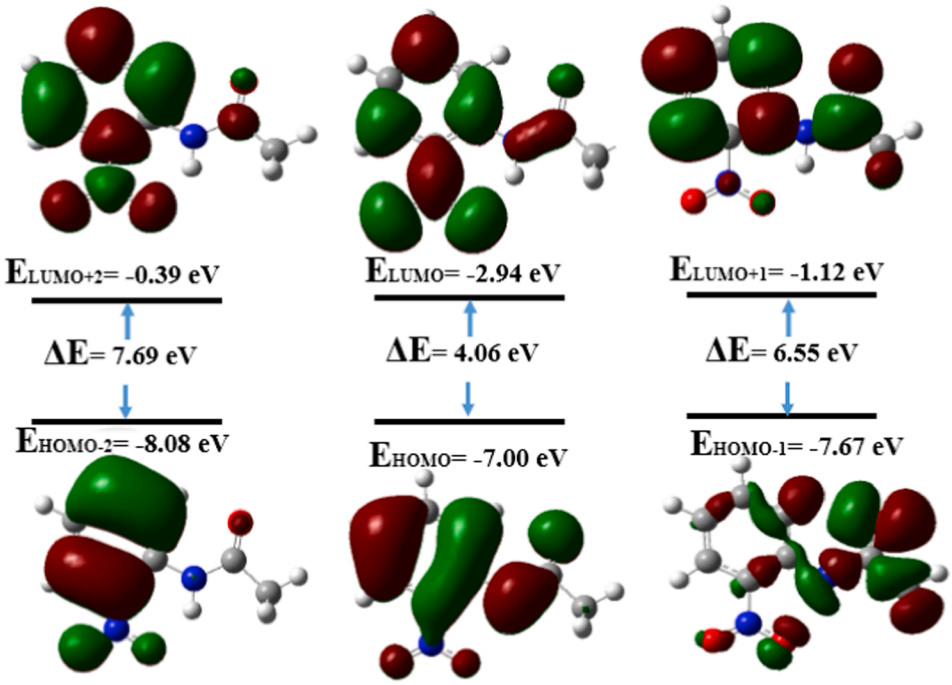

Fig. 4. The frontier molecular orbitals of ***o*-NAA** computed using the B3LYP/6-311G (d,p) method.

Table 7
Calculated quantum chemical molecular orbital properties for ***o*-NAA**.

Parameters	DFT/B3LYP	
	6-31G(d,p)	**6-311G(d,p)**
E_{HOMO} (eV)	−6.77	−7.00
E_{LUMO} (eV)	−2.74	−2.94
$E_{HOMO} - E_{LUMO}$ (eV)	4.03	4.06
I_P (eV)	6.77	7.00
E_A (eV)	2.74	2.94
χ (eV)	4.75	4.97
η (eV)	2.01	2.03
S (eV^{-1})	1.01	1.02
P (eV)	−4.75	−4.97
ω (eV)	5.61	6.08

the physical/chemical properties in chemical structures [64]. In order to predict the reactive sites of the electrophilic or nucleophilic attack for the investigated compound, its MEP was calculated at the B3LYP/6 − 31G(d,p) and B3LYP/6 − 311G(d,p) levels. These sites give information about the region from where the compound can have intermolecular interactions. Mathematically, MEP can be defined by the following equation:

$$V_{(r)} = \sum \left(\frac{Z_A}{R_A} - r\right) - \int (p(r')/r' - r)dr'$$

With Z_A is the nucleus charge which is located at R_A and $\rho(r')$ is the electron density.

Different standard colors such as red, orange, yellow, green and blue are used in the MEP frame to explain the degree of the electrostatic potential which increases in this order red < orange < yellow < green <

Table 8
Electric dipole moment (μ), static linear polarizability (α), static first-order hyper polarizability (β) and static second-order hyper polarizability (γ) values of ***o*-NAA** in gas phase.

NLO parameters	DFT/B3LYP		NLO parameters	DFT/B3LYP	
	6-31G(d,p)	**6-311G(d,p)**		**6-31G(d,p)**	**6-311G(d,p)**
Dipole moment			β_{yyy}	−377.998	0.081
μ_x	−0.01453	0.0	β_{xxz}	0.007	14.874
μ_y	−0.00178	0.0	β_{yxz}	−0.024	−0.169
μ_z	1.29300	1.32949	β_{yyz}	0.026	−16.126
μ	**1.29309**	**1.32949**	β_{zxz}	−5.491	191.241
Polarizability			β_{zyz}	−25.825	0.818
α_{xx}	154.262	159.613	β_{zzz}	−0.036	−382.096
α_{xy}	4.232	0.203	**$\beta_{\|\|}$ (au)**	**267.587**	**257.653**
α_{yy}	133.601	51.195	**$\beta_{\|\|}\times10^{-30}$ (esu)**	**2.312**	**2.226**
α_{zx}	0.011	5.037	*Second-order hyperpolarizability*		
α_{zy}	0.002	−0.104	γ_{xxxx}	30041.1	36860.6
α_{zz}	44.100	137.823	γ_{yyyy}	199.566	878.684
α (au)	**110.654**	**116.210**	γ_{zzzz}	15342.4	18755.3
α × 10^{-24} (esu)	**16.397**	**17.221**	γ_{xxyy}	188.462	671.953
First-order hyperpolarizability			γ_{xxzz}	5749.29	7206.92
β_{xxx}	43.5835	7.744	γ_{yyzz}	140.667	690.282
β_{xxy}	20.4467	0.013	**⟨γ⟩ (au)**	**11547.981**	**14726.579**
β_{yxy}	189.765	−05.474	**⟨γ⟩ × 10^{-36} (esu)**	**5.82**	**7.42**

blue. Furthermore, the red color represents the most negative electrostatic potential and the favored site for the electrophilic reactivity, as shown in Fig. 5. On the other hand, the nucleophile loving site with most positive potential is indicated by blue color [65,66]. The studied molecule has several possible sites for electrophilic attacks at the O1, O2 and O3 atoms which are highlighted as red-colored zones. Moreover, the MEP drawing shows that the positive potential sites illustrated in green are around the hydrogen atoms indicating the electron deficient zone which implies that the encounter of nucleophilic can take place on this region.

3.9. Thermodynamic properties

For a better understanding of ***o*-NAA** properties, the correlations between the statistical thermodynamics and the temperature were also obtained (Table 9 and Fig. 6). It can be seen that the heat capacities, the entropies and the enthalpies increase when increasing the temperature of a molecule, as well as the intensity of the molecular vibrations. The standard statistical thermodynamic functions such as the standard heat capacities, the standard entropies and the standard enthalpy changes (0 → T) were obtained and are listed in Table 9. Hence, the standard heat capacities, the entropies and the enthalpy changes increase at any temperature ranging from 100 to 1000 K. By increasing, the temperature causes also an increase in the intensity of the molecular vibration. The correlation graphs are shown in Fig. 6. All the thermodynamic data supply helpful information for the understanding of ***o*-NAA**. Consequently, these data can be used to compute other thermodynamic energies according to the thermodynamic functions relationships and can also estimate directions of chemical reactions according to the second law of thermodynamics in thermochemical field [67].

3.10. Hirshfeld surface and energy frameworks analyses

Hirshfeld surface analysis is a powerful tool used to understand the intermolecular interactions nature within a crystal structure. The function d_{norm} displays a surface with a red–white–blue-colored scheme, in which the white color represents the contacts around the *van der Waals* radii, while the red and blue-colored are as indicate the shorter and longer intermolecular contacts of the molecule, respectively. It was generated using a standard high surface resolution with the 3D isosurface mapped over a fixed color scale of −0.2522 (red) to 1.0523 Å (blue). Consequently, *Hirshfeld* surfaces **HSs** and their subsequent 2D-fingerprint plots **FPs** were calculated in order to quantify and analyze the intermolecular contacts present within the crystal structure of ***o*-NAA** and their associated energy frameworks **EFs**, using CrystalExplorer17 [34], which will help understanding both their geometry and strength.

Table 9
Thermodynamic properties for ***o*-NAA**.

T(K)	B3LYP/6-31G(d,p)			B3LYP/6-311G(d,p)		
	S(J/mol.k)	Cp(J/mol.k)	ddH(kj/mol)	S(J/mol.k)	Cp(J/mol.k)	ddH(kj/mol)
100	295.38	72.20	4.86	293.65	69.98	4.76
200	360.43	120.91	14.52	357.65	119.22	14.21
293	414.66	165.82	27.86	410.88	164.47	27.42
298	417.57	168.26	28.72	413.76	166.90	28.27
300	418.62	169.13	29.03	414.80	167.77	28.58
400	473.57	214.26	48.25	469.28	212.20	47.62
500	525.71	253.41	71.68	520.83	250.04	70.80
600	574.88	285.88	98.70	569.26	281.01	97.40
700	621.01	312.42	128.66	614.52	306.09	126.80
800	664.20	334.15	161.03	656.78	326.53	158.47
900	704.62	352.13	195.37	696.24	343.41	191.99
1000	742.53	367.21	231.36	733.18	357.56	227.06

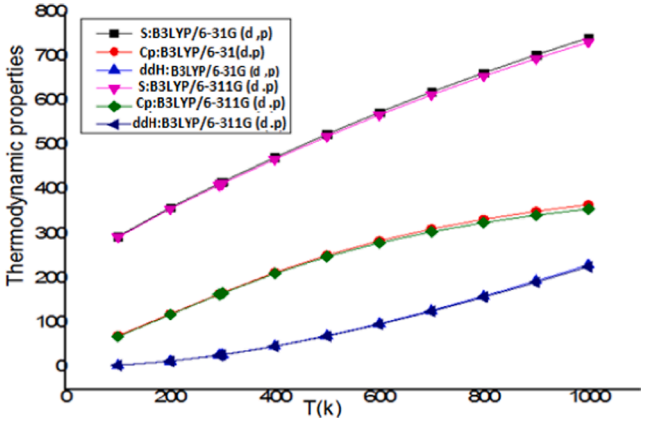

Fig. 6. Correlation graph of the thermodynamic parameters for ***o*-NAA.**

By partitioning the complete **FP** provided in Fig. 7.a into the decomposed **FPs** related to the contribution of each contact type separately, it can be seen that the crystal packing of ***o*-NAA** is mainly dominated by H…H contacts followed by H…O/O…H contacts with the largest two contributions over the total **HS** of 35.3% (Fig. 7.b) and 28.6% (Fig. 7.c), respectively.

It is of interest to point out that the H…H contacts situated in the middle of the scattered points in the FP (Fig. 7.b) display a high concentration at about $d_i = d_e \sim 1.2$ Å associated to both reciprocal H6…H8a/H8a…H6 and H4…H8b/H8b…H4 contacts displayed as two

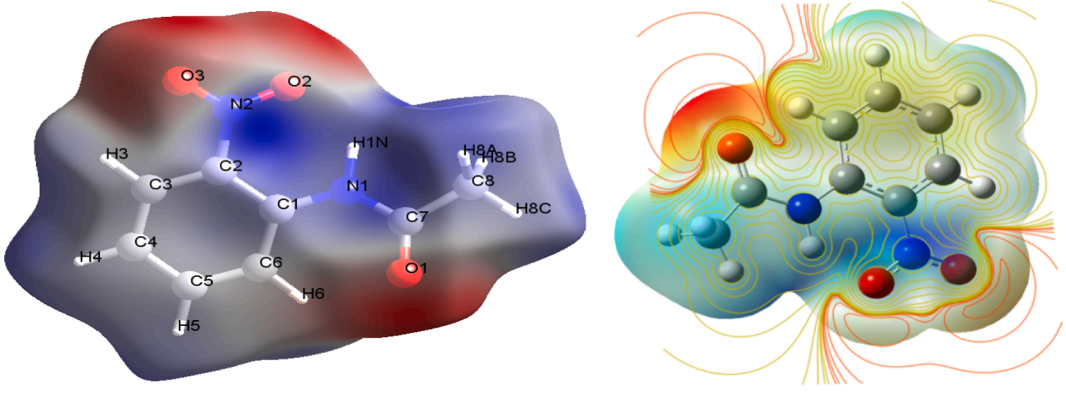

(a) **(b)**

Fig. 5. (a) MEP surface and (b) 2D contour map for ***o*-NAA.**

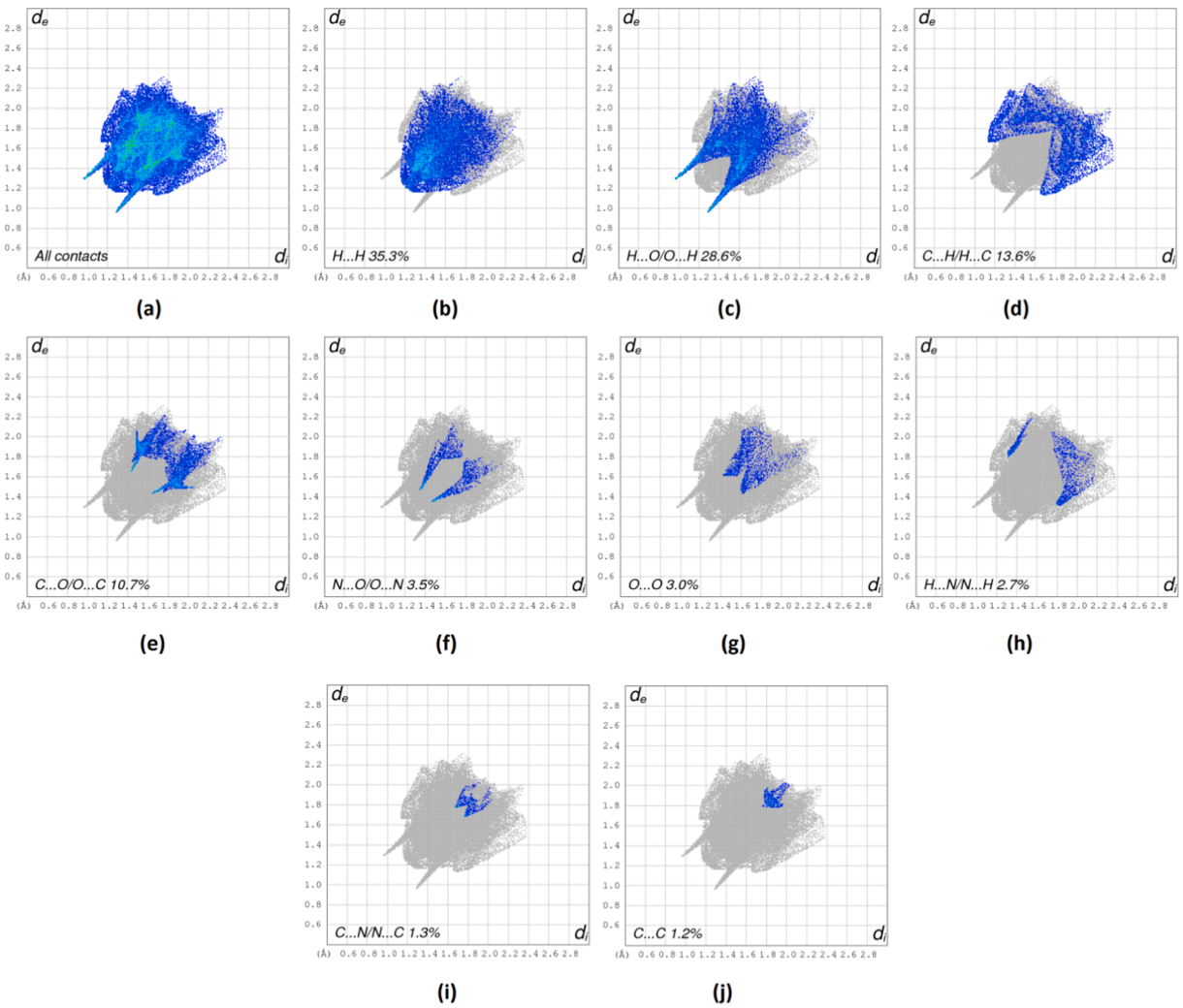

Fig. 7. The 2D-FP plots showing the overall contribution to the total **HS** area and the individual percentages of the diverse intermolecular contacts of ***o*-NAA.**

orange spots mapped on the d_i (or d_e) representation (Fig. 8.a and Fig. 8. b), which indicates that they are significant short range H…H contacts. Furthermore, the H…O/O…H contacts appearing as two sharp spikes in the **FP** (Fig. 7.c) are highlighted in Fig. 8.c and Fig. 8.d as large bright red spots plotted on the d_{norm} function. These two spikes are indicative of strong intermolecular hydrogen-bonding interactions resulting from the O1 atom acting as a double acceptor in the two reciprocal interactions C5—H5…O1/O1…H5—C5 and C8—H8c…O1/O1…H8c—C8, being respectively 2.1 Å and 2.26 Å long.

The second two contributors among the interacting atoms to the total **HS** area are the H…C/C…H (Fig. 7.d) and C…O/O…C (Fig. 7.e) contacts, thus covering 13.6% and 10.7 % of the global surface, respectively. Two large lateral points distribution in the vicinity of $d_i + d_e \sim 2.8$ Å were observed for the H…C/C…H contacts and were associated to the shortest C4—H4…C3/C3…H4—C4 intermolecular interactions visualized on the d_i surface (Fig. 8.a). Furthermore, the **HS** mapped over d_i exhibits an additional short H…C/C…H contact appearing at around $d_i + d_e \sim 3.28$ Å, and attributed to the N1—H1…C6 interaction (Fig. 8.a) and its reciprocal C6…H1—N1 (Fig. 8.b).As for the shortest C…O/O…C contacts, they reveal the existence of π…*lp*/*lp*…π interactions resulting from the reciprocal C7…O3/O3…C7 contacts ($d_i + d_e \sim 3.10$ Å), which were displayed on the **HS** mapped on d_{norm} (Fig. 8.d) as small light-red spots between the subsequent donors and acceptors.

Regardless of the contributions of the remaining observed contacts towards the crystal packing of **o-NAA**, which were found to be less than 4%, they represent short non-classical interactions contributing to the stabilization of the studied molecule crystal packing. Therefore, the O2 atom was found to be involved in many *lp*…*lp* interactions resulting *inter alia* from the N…O/O…N contacts which contribute to 3.5% (Fig. 7.f) of the total *Hirshfeld* area. This is consequently confirmed by the **HS** exhibited by representing the d_{norm} function which showed the reciprocal shortest interactions N2…O2/O2…N2 (Fig. 8.d) appearing as medium bright-red spots at $d_e + d_i \sim 2.88$ Å. Additionally, the O2 oxygen interacts with O1 and O3 thus yielding to O…O contacts, which cover 3.0% (Fig. 7.g), and resulting in other short *lp*…*lp* interactions, being respectively 3.02 Å and 3.08 Å long. As shown in (Fig. 9.a) visualized on the *shape index* representation, the two reciprocal short O2…O1/O1…O2 and O2…O3/O3…O2 contacts are noticeable as big orange spots.

It is worth to be noted that another type of non-conventional contacts was observed in the crystal structure of **o-NAA**, namely H…N/N…H contacts which witnesses of the occurrence of C—H…N/N…H—C interactions through the shortest contact between H6 and N1 being approximately 3.12 Å long, with a percentage of 2.7% towards the full **HS** (Fig. 7.h). Moreover, a contribution of 1.3% (Fig. 7.i) was observed for the N…C/C…N contacts through the subsequent N2 and C5 atoms which appear to be the shortest *lp*…π/π…*lp* interaction of about 3.48 Å long. (Fig. 7.j) illustrates the distribution of the C…C contacts of 1.2% presented as small scattering points in the upper corner of the total FP plot, which could be attributed to the π…π stacking resulting mainly from the interaction of the C2 and C6 atoms and corresponding to a short length of around 3.64 Å. The three interactions types are highlighted in

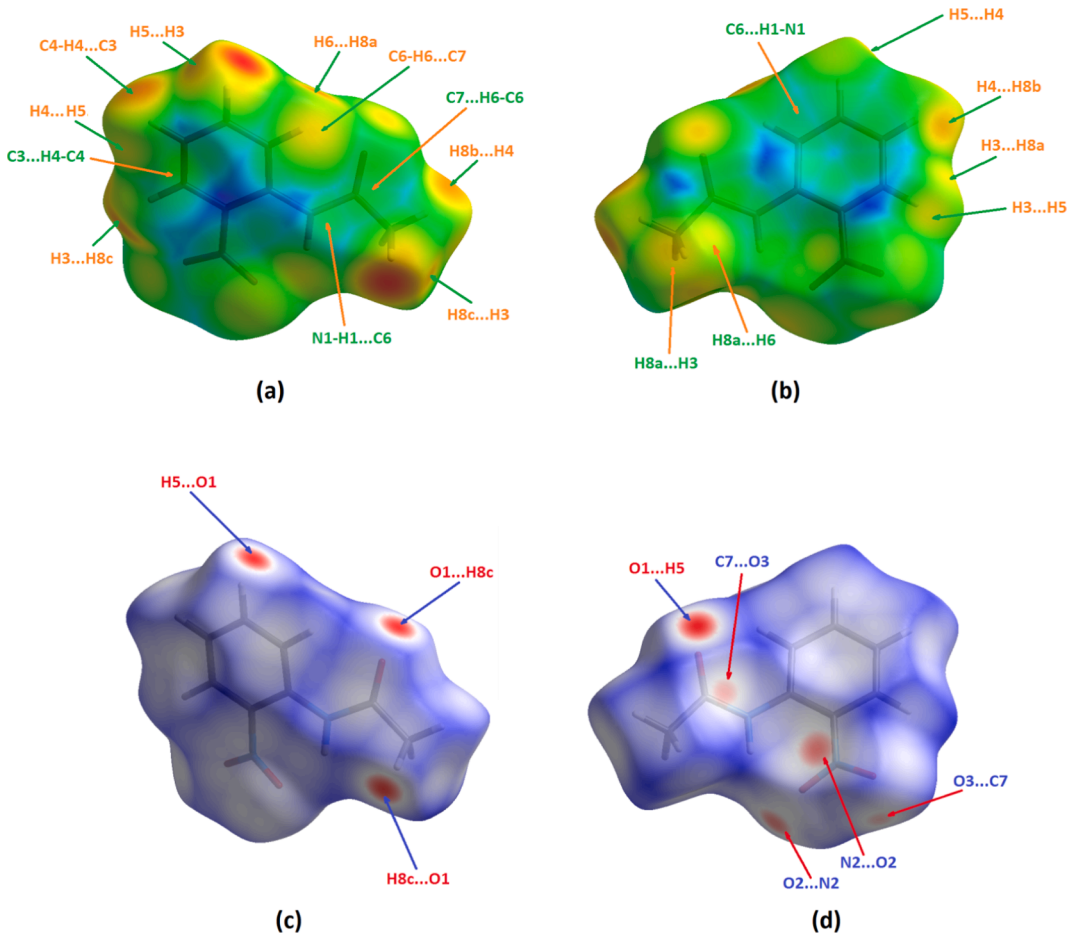

Fig. 8. (a) Shortest H…H contacts mapped over the d_i function, and (b) **HS** mapped on d_{norm} visualizing the shortest C—H…O/O…H—C hydrogen bonds.

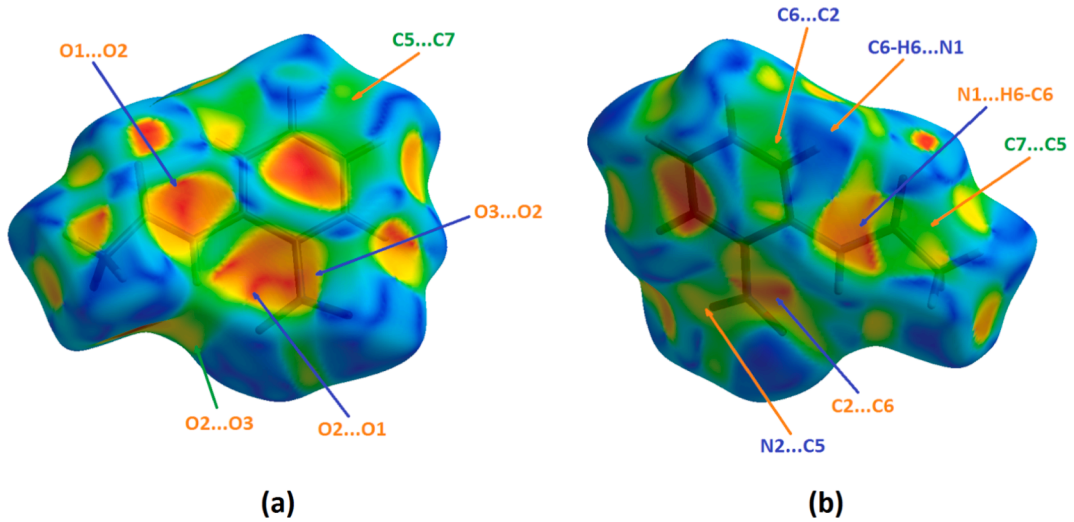

Fig. 9. *Shape index* representation showing (a) the *lp*…π/π…*lp*, (b) the π…π and the C—H…N/N…H—C interactions occurring within the crystal packing of ***o*-NAA.**

(Fig. 9) by showing a *shape index* representation of the **HS**.

An energy frameworks **EFs** analysis [68,69] was adopted serving as a comprehensive study of the interactions topology and their strength in the crystal packing of **o-NAA**. Therefore, the molecules clusters were generated within a radius of 3.8 Å around the central molecule and the interaction energies **IEs** between pairs of molecules were performed based on the CE-B3LYP/6-31G(d,p) level of theory. The total **IE** is obtained by the combination of the electrostatic energy E_{ele}, the exchange repulsion energy E_{rep}, the polarization energy E_{pol} and the dispersion energy E_{dis} [69,70].

Table 10 shows the results of the **IE** calculations for **o-NAA** provided by respective colors. While the overall energies of the possible intermolecular interactions in the crystal packing are found to be in the range [−0.3, −26.8] kJ·mol^{-1}, the *lattice energy* of the studied molecule equals

Table 10
Interaction energies (kJ/mol) in ***o*-NAA**. *N* refers to the number of molecules with an *R* molecular centroid-to-centroid distance (Å).

	N	Primary interaction	Symmetry code	*R*	*E*'ele	*E*'pol	*E*'dis	*E*'rep	*E*'tot
	2	C4—H4…C3	-*x*+½,*y*+½,-*z*+½	7.78	-1.0	-0.7	-12.7	8.8	-7.2
	2	π…*lp* (C7…O3) *lp*…*lp* (N2…O2) *lp*…*lp* (O2…O3)	-*x*+½,*y*+½,-*z*+½	5.05	-12.9	-3.8	-24.4	17.7	-26.8
	2	N1—H1…C6 *lp*…*lp* (O2…O1) *lp*…π (N2…C5) C8—H8c…O1 π…π (C2…C6)	*x*,*y*,*z*	4.98	-11.9	-2.8	-28.6	22.7	-25.5
	2	H3…H8b	*x*+½,-*y*+½,*z*+½	9.20	-1.2	-0.7	-8.6	7.0	-5.0
	1	C6—H6…N1	-*x*,-*y*,-*z*		1.6	-0.9	-24.8	9.9	-14.5
	2	H4…H8b	*x*+½,-*y*+½,*z*+½	5.77	-4.5	-1.4	-9.2	5.7	-10.3
	1	C5—H5…O1	-*x*,-*y*,-*z*	9.05	-19.7	-4.6	-13.1	21.5	-22.3
	1	π…π (C8…C8)	-*x*,-*y*,-*z*	7.41	1.1	-0.1	-1.5	0.1	-0.3
	1	H8a…H8b	-*x*,-*y*,-*z*	9.47	-0.1	-0.4	-5.4	2.4	-3.6

– 95.15 kJ·mol^{-1}. From Table 10, it can be seen that the orange-colored molecule being at a distance of 5.05 Å from the centroid of the selected molecule with symmetry operation (-*x*+½,*y*+½,-*z*+½) presented the highest total interaction energy E_{tot} of – 26.8 kJ·mol^{-1}. Whereas, the purple-colored one, with the symmetry code (-*x*,-*y*,-*z*), positioned at about 7.41 Å from the same centroid displayed the lowest total interaction energy of – 0.3 kJ·mol^{-1}.

The energy framework **EF** diagrams through the *b*-axis are graphically illustrated in Fig. 10 with respect to the symmetry-coded molecules around the central one. The **IE** components and their distribution pattern in the framework revealed that the dispersion energy is the dominate component in the crystal packing of ***o*-NAA**.

From Table 10 and Fig. 10, it can be concluded that the much stronger intermolecular interactions have the highest **IEs** which are shared between the pair-molecules related through the non-classical (π…*lp*, *lp*…*lp*) and (C—H…O, N—H…C, *lp*…*lp*, *lp*…π, π…π) interactions with total **IEs** of – 26.8 kJ·mol^{-1} and – 25.5 kJ·mol^{-1}, respectively. Both **IEs** are graphically visualized as large cylinders along the [1 0 1] direction and the *b*-axis, respectively. The involved molecular pairs are primarily stabilized by the dispersion and repulsion components. Additionally, these interactions are followed by the C—H…O hydrogen bond highlighted by large tubes running through the [1 1 0] direction and mainly stabilized by the electrostatic and repulsive components, with a total **IE** being – 22.3 kJ·mol^{-1}. Whereas, the remaining weak interactions are found to be interconnecting the large cylindrical tubes crosswise.

4. Conclusions

In the present work, synthesis, characterization by single-crystal XRD, FTIR, UV–visible, ^{1}H NMR and ^{13}C NMR spectroscopic studies of ***o*-NAA** were reported. Furthermore, the molecular geometry, the vibrational frequencies and the infrared intensities of the molecule in the ground state were calculated by using the DFT/B3LYP method with

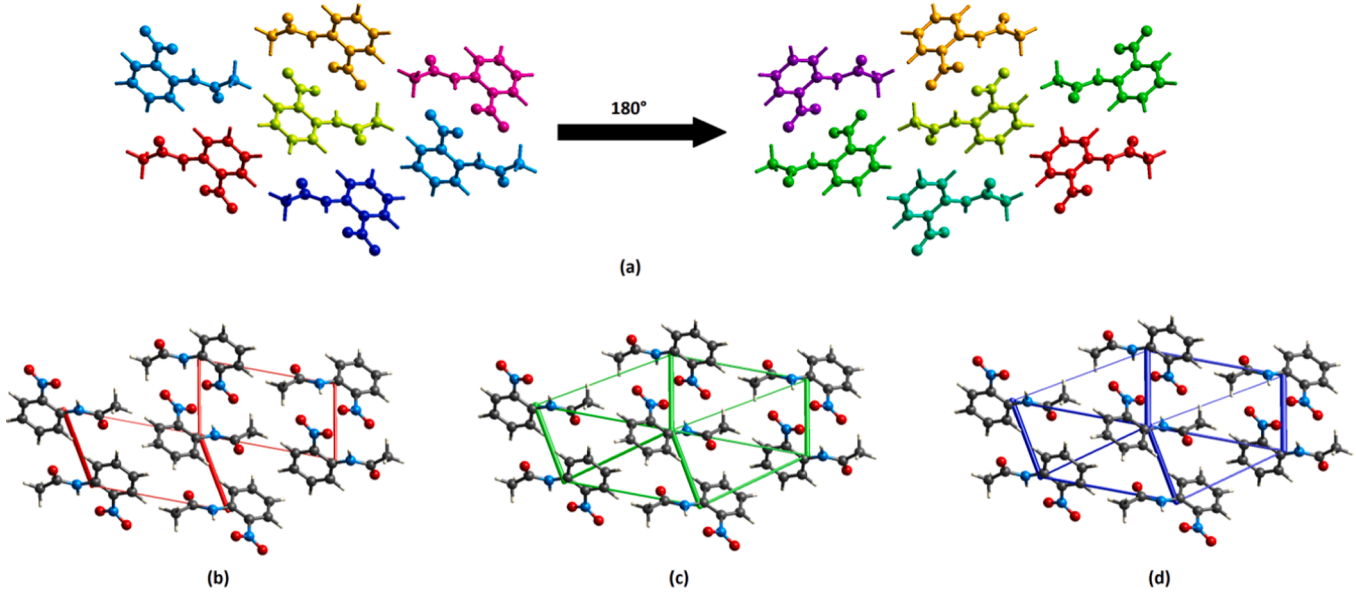

Fig. 10. (a) Symmetry-coded molecules in ***o*-NAA** and their energy frameworks: (b) electrostatic, (c) dispersion and (d) total energies.

the 6 − 31G(d,p) and 6 − 311G(d,p) basis sets. The assignments of all the fundamental modes of the reported molecule were made unambiguously based on the results of the PED output. It was found that both levels reproduce very well the geometry and the properties of the molecule. Additionally, the experimentally observed and theoretically calculated ^{1}H and ^{13}C NMR chemical shifts were similarly compared and found to be in a very good agreement. On the other hand, the estimation of the UV–Visible spectrum of ***o*-NAA** has proven that the maximum absorption wavelength could be associated to the n → π* electronic transition. The frontier orbital energies were evaluated explaining the charge transfer interactions taking place within the molecule. The reactivity of ***o*-NAA** was further estimated by computing the global chemical reactivity descriptors. Moreover, calculated Mulliken atomic charges of the studied molecule were computed and discussed, and the thermodynamic properties were estimated with the DFT method using the same basis set. The calculated molecular electrostatic potential (MEP) map has as expected shown that the negative potential sites are on the electronegative atoms,whereas the positive potential sites are around thehydrogen atoms. These sites give information about the possibleareas for inter- and intramolecular hydrogen bonding.The NLO properties of ***o*-NAA** were theoretically investigated by estimating the dipole moment, the polarizability, the first and second-order hyperpolarizabilities at B3LYP/6-31G(d,p) and B3LYP/6-311G(d,p) levels of theory. Theoretical calculations carried out using the 6-311G(d,p) basis set gave better results for dipole moment (1.329 D), polarizability (17.22×10^{-24} esu) and second-order hyperpolarizabilities (7.42×10^{-36} esu) compared to the results obtained by the 6-31G(d,p) basis set. The values of the average second hyperpolarizability are found almost similar to urea (4.16×10^{-36} esu). To show that the molecule of *o*-NAA exhibits a huge third-order nonlinearity, the dynamic polarizability and hyperpolarizabilities were also predicted. The obtained values have thus demonstrated that the studied molecule has a promising NLO behavior. The *Hirshfeld* surface analysis and the subsequent 2D-fingerprint plots have indicated that it was clear that the H…H, H…O/O…H, H…C/C…H and C…O/O…C contacts, were the most significant contributors among the interacting atoms. However, the N…O/O…N, O…O, H…N/N…H, N…C/C…N and C…C close contacts have played an interesting role in stabilizing the crystal structure of the studied molecule, which was proved by computing the intermolecular energies. Furthermore, the crystal packing of ***o*-NAA** was further analyzed in terms of 3D-molecular energy frameworks, in order to get quantitative insights into the intermolecular interactions nature and their strength. The obtained results have therefore demonstrated the significance of the much stronger intermolecular interactions, namely C—H…O, N—H…C, *lp*…*lp*, *lp*…π and π…π, in stabilizing the packing of ***o*-NAA**.

CRediT authorship contribution statement

Nourdine Boukabcha: Writing – original draft, Visualization, Investigation. **Amani Direm:** Writing – original draft, Writing – review & editing, Visualization, Validation. **Mokhtaria Drissi:** Writing – original draft, Visualization. **Youcef Megrouss:** Writing – original draft, Visualization. **Nawel Khelloul:** Writing – original draft, Visualization. **Necmi Dege:** Writing – original draft, Resources, Investigation. **Murat Tuna:** Writing – original draft, Resources, Investigation. **Abdelkader Chouaih:** Conceptualization, Supervision, Resources, Validation, Writing – original draft.

Declaration of Competing Interest

The authors declare that they have no known competing financial interests or personal relationships that could have appeared to influence the work reported in this paper.

Acknowledgements

The authors gratefully acknowledge the financial support via PRFU project from The Algerian Ministry of Higher Education and Scientific Research, the Directorate General of Scientific Research and Technological Development (DGRSDT), and Abdelhamid Ibn Badis University of Mostaganem.

Appendix A. Supplementary material

Crystallographic data for the structure reported in this article have been deposited with Cambridge Crystallographic Data Center, CCDC 2090679. Copies of this information may be obtained free of charge from the Director, CCDC, 12 Union Road, Cambridge, CBZ IEZ, UK. Facsimile (44) 01223 336 033, E-mail: deposit@ccdc.cam.ac.uk or http//www.ccdc.com.ac.uk/deposit. Supplementary data to this article can be found online at https://doi.org/10.1016/j.inoche.2021.108884.

References

[1] R.C. Weast (Ed.), CRC Handbook of Chemistry and Physics, 62nd ed.,, CRC Press, Boca Raton, FL, 1981, p. p. C-67..
[2] A. Bertolini, A. Ferrari, A. Ottani, S. Guerzoni, R. Tacchi, S. Leone, CNS Drug Rev. 12 (2006) 250.
[3] Y. Baena, J.A. Pinzon, H.J. Barbosa, F. Martinez, Temperature-dependence of the solubility of some acetanilide derivatives in several organic and aqueous solvents, Phys. Chem. Liq. 42 (2004) 603.
[4] P. Hamm, G.P. Tsironis, Semiclassical and quantum polarons in crystalline acetanilide, Eur. Phys. J., Spec. Top. 147 (2007) 303.
[5] J.L. Pereira, C.J. Hill, R.M. Sibly, V.N. Bolshakov, F. Goncalves, L.H. Heckmann, A. Callaghan, Aquat. Toxicol. 97 (2010) 268.
[6] E.F. Larit, M. Litim, H. Akkari, Acetanilide Compounds as Corrosion Inhibitors for 304L Stainless Steel in 1 M HCl Solution, Anal. Bioanal. Electrochem. 11 (1) (2019) 49–58.
[7] D. Chemla, J. Zyss, Nonlinear Optical Properties of Organic Molecules and Crystals, Academic Press Inc, NewYork, 1987.
[8] S. Senthil, J. Madhavan, X-ray diffraction. Spectroscopic and mechanical studies on potential organic NLO materials of Meta-Nitroaniline and N-3-Nitrophenyl Acetamide single crystals, IOP Conf, Series, Mater. Sci. Eng. 73 (2015), 012110.
[9] J. Zyss, Molecular Nonlinear Optics: Materials, Physics and Devices (Quantum Electronics-Principles and Applications), Academic Press Inc, Boston, 1994.
[10] T. Kaino, B. Cai, K. Takayama, Adv. Funct. Mater. 12 (2002) 599–603.
[11] W. Geis, R. Sinta, W. Mowers, S.J. Deneault, M.F. Marchant, K.E. Krohn, S. J. Spector, D.R. Calawa, T.M. Lyszczarz, Appl. Phys. Lett. 84 (2004) 3729–3731.
[12] A. Schneider, M. Neis, M. Stillhart, B. Ruiz, R.U.A. Khan, P. Gunter, J. Opt. Soc. Am. B 23 (2006) 1822–1835.
[13] J. Zyss (Ed.), Molecular Nonlinear Optics: Materials, Physics, and Devices, Academic Press, New York, 1994.
[14] B. Ferguson, Z.-C. Zhang, Nat. Mater. 1 (2002) 26–33.
[15] M. Lenin, P. Ramasamy, Synthesis, growth and characterization of 3-nitroacetanilide A new organic nonlinear optical crystal by Bridgman technique, J. Cryst. Growth 310 (2008) 4451.
[16] N. Boukabcha, N. Benhalima, R. Rahmani, A. Chouaih, F. Hamzaoui, Theoretical investigation of electrostatic potential and non linear optical properties of Meta–nitroacetanilide, R J Chem 8 (2015) 509.
[17] T. Gnanasambandan, S. Gunasekaran, S. Seshadri, Experimental and theoretical study of p-nitroacetanilide, Spectrochim. Acta Part A Mol. Biomol. Spectrosc. 117 (2014) 557–567.
[18] C.R. Groom, I.J. Bruno, M.P. Lightfoot, S.C. Ward, The Cambridge Structural Database. Acta Cryst. B72 (2016) 171–179.
[19] S. Kashino, T. Matsushita, T. Iwamoto, K. Yamaguchi, M. Haisa, Structure of N-Aromatic Amides, II. XC6H4NHCOY, Acta Cryst. C42 (1986) 457–462.
[20] X. He, J.G. Stowell, K.R. Morris, R.R. Pfeiffer, H. Li, G.P. Stahly, S.R. Byrn, Stabilization of a Metastable Polymorph of 4-Methyl-2-nitroacetanilide by Isomorphic Additives, Cryst. Growth Des. 1 (4) (2001) 305–312.
[21] J.-Y. Qi, Z.-Y. Zhou, D.-S. Liu, A.S.C. Chan, 4'-Fluoro-2'-nitro-acetanilide, Acta Cryst. E57 (2001) o675–o676.
[22] J.C. Moore, A. Yeadon, R.A. Palmer, Crystal and molecular structures of two polymorphs of 4-methyl-2-nitroacetanilide (MNA), J. Crystallogr. Spectrosc. Res. 13 (1983) 279–292.
[23] J.C. Moore, A. Yeadon, R.A. Palmer, Crystal and molecular structure of an amber polymorph of 4-methyl-2-nitroacetanilide (MNA), J. Crystallogr. Spectrosc. Res. 14 (1984) 283–291.
[24] C. Zalaru, M.R. Caira, M. Iovu, E. Cristea, X-ray structures of new substituted 2-(pyrazol-1-yl)-2′-nitroacetanilides with pharmacological activity, J. Chem. Crystallogr. 34 (2004) 317–324.
[25] Stoe & CieX-AREA (Version 1.18) and X-RED32 (Version 1.04), Stoe & Cie, Darmstadt, Germany, (2002).
[26] G.M. Sheldrick, A Short History of SHELX, Acta Cryst A 64 (2008) 112–122.

[27] G.M. Sheldrick, Crystal structure refinement with SHELXL, Acta Cryst A 71 (2015) 3–8.
[28] A.L. Spek, Structure validation in chemical crystallography, Acta Cryst D 65 (2009) 148–155.
[29] C.F. Macrae, P.R. Edgington, P. McCabe, E. Pidcock, G.P. Shields, R. Taylor, M. Towler, Mercury: visualisation and analysis of crystal structures, J. Appl. Cryst. 39 (2006) 453–457.
[30] M.J. Frisch , G.W. Trucks , H.B. Schlegel , G.E. Scuseria , M.A. Robb , J.R. Cheeseman , G. Scalmani , V. Barone , B. Mennucci , G.A. Petersson , H. Nakatsuji , M. Caricato , X. Li , H.P. Hratchian , A.F. Izmaylov , J. Bloino , G. Zheng , J.L. Sonnenberg , M. Hada , M. Ehara , K. Toyota , R. Fukuda , J. Hasegawa , M. Ishida , T. Nakajima , Y. Honda , O. Kitao , H. Nakai , T. Vreven , J.A. Montgomery Jr. , J.E. Peralta , F. Ogliaro , M. Bearpark , J.J. Heyd , E. Brothers , K.N. Kudin , V.N. Staroverov , T. Keith , R. Kobayashi , J. Normand , K. Raghavachari , A. Ren- dell , J.C. Burant , S.S. Iyengar , J. Tomasi , M. Cossi , N. Rega , J.M. Millam , M. Klene , J.E. Knox , J.B. Cross , V. Bakken , C. Adamo , J. Jaramillo , R. Gom- perts , R.E. Stratmann , O. Yazyev , A.J. Austin , R. Cammi , C. Pomelli , J.W. Ochter- ski , R.L. Martin , K. Morokuma , V.G. Zakrzewski , G.A. Voth , P. Salvador , J.J. Dannenberg , S. Dapprich , A.D. Daniels , O. Farkas , J.B. Foresman , J.V. Ortiz , J. Cioslowski , D.J. Fox , Gaussian 09, Revision B.01, Gaussian, Inc., Wallingford CT, 2009.
[31] R. Dennington. T. Keith. J. Millam: Semichem Inc, Shawnee Mission KS. GaussView. Version 5, 2009.
[32] A. Becke, Density-functional thermochemistry. III, The role of exact exchange, J. Chem. Phys. 98 (1993) 5648.
[33] M. H. Jamróz, Vibrational Energy Distribution Analysis VEDA 4, Warsaw, 2004.
[34] M.J. Turner, J.J. MacKinnon, S.K. Wolff, D.J. Grimwood, P.R. Spackman, D. Jayatilaka, M.A. Spackma. Crystal Explorer Ver. 17.5. University of Western Australia, (2017). http://crystalexplorer.scb.uwa.edu.au.
[35] D. Avci, H. Cömert, Y. Atalay, J. Mol. Model. 14 (2008) 161.
[36] R.M. Silverstein, F.X. Webster, Spectrometric Identification of Organic Compounds, Jon Wiley Sons Inc, New York, 1963 pp 72.
[37] J.B. Lambert, H.F. Shurvell, L. Verbit, R.G. Cooker, G.H. Stout; Organic Structural Analysis pp 235, (2009).
[38] R.N. Singh, A. Kumar, P. Rawat, R.K. Tiwari, A.K. Singh, Studies on molecular structure. spectral analysis. Chemical reactivity and first hyperpolarizability of a newly synthesized 1,9-bis[(4-isonicotinoyl)-hydrazonomethyl]-5-phenyl-dipyrromethane using experimental and theoretical approaches, J. Mol. Struct. 67 (2013) 1052.
[39] M.R. Anoop, P.S. Binil, S. Suma, M.R. Sundarsanakumar, S. Mary, H.T. Varghese, C. Y. Panicker, J. Mol. Struct. 969 (2010) 48.
[40] K.C. Medhi, R. Barman, M.K. Sharma, Indian J. Phys. B 68 (1994) 189.
[41] Y. Megrouss, F.T. Baara, N. Boukabcha, A. Chouaih, A. Hatzidimitriou, A. Djafri, F. Hamzaoui, Synthesis, X-Ray Structure Determination and Related Physical Properties of Thiazolidinone Derivative by DFT Quantum Chemical Method, Acta Chim. Slov. 66 (2019).
[42] V. Krishnakumar, R.J. Xavier, Spectrochim. Acta, Part A 60 (2004) 709.
[43] S. George, Infrared and Raman Characteristic Group Frequencies — Tables and Charts, Third Ed, Wiley, New York, 2001.
[44] J.R. Cheeseman, G.W. Trucks, T.A. Keith, M.J. Frisch, J. Chem. Phys. 104 (1996) 5497.
[45] N. Boukabcha, A. Djafri, Y. Megrouss, Ö. Tamer, D. Avci, M. Tuna, N. Dege, A. Chouaih, Y. Atalay, A. Djafri, F. Hamzaoui, Synthesis, crystal structure, spectroscopic characterization and nonlinear optical properties of (Z)-N'-(2,4-dinitrobenzylidene)-2(quinolin-8-yloxy) acetohydrazide, J. Mol. Struct. 1194 (2019) 112–123.
[46] C.M. Rohlfing, L.C. Allen, R. Ditchfield, Chem. Phys. 87 (1984) 9.
[47] D. Avcı, Y. Atalay, Effects of different GIAO and CSGT models and basis sets on 2-aryl-1.3.4-oxadiazole derivatives, J. StructChem 20 (2009) 185.
[48] P. Politzer, F. Abu-Awwad, A comparative analysis of Hartree-Fock and Kohn-Sham orbital energies, Theor. Chem. Acc. 99 (1998) 83.
[49] R.S. Mulliken, A New Electroaffinity Scale; Together with Data on Valence States and on Valence Ionization Potentials and Electron Affinities, J. Chem. Phys. 2 (1934) 782.
[50] R.G. Pearson, Absolute electronegativity and hardness: applications to organic chemistry, J. Org. Chem. 54 (1989) 1423.
[51] R.G. Pearson, Chemical Hardness-Applications from Molecules to Solids, John Wiley–VCH, Weinheim, 1997.
[52] N.E.H. Belkafouf, F. Triki-Baara, A. Altomare, R. Rizzi, A. Chouaih, A. Djafri, F. Hamzaoui, Synthesis, PXRD structural determination, Hirshfeld surface analysis and DFT/TD-DFT investigation of 3N-ethyl-2N'-(2-ethylphenylimino) thiazolidin-4-one, J. Mol. Struct. 1189 (2019) 8–20.
[53] J. Padmanabhan, R. Parthasarathi, V. Subramanian, P.K. Chattaraj, J. Phys. Chem. 111 (2007) 1358.
[54] Y.X. Sun, Q.L. Hao, W.X. Wei, Z.X. Yu, L.D. Lu, X. Wang, Y.S. Wang, Experimental and density functional studies on 4-(3. 4-dihydroxybenzylideneamino) antipyrine. and 4-(2. 3. 4-trihydroxybenzylideneamino) antipyrine, J. Mol. Struct. 904 (2009) 74–82.
[55] C. Andraud, T. Brotin, C. Garcia, F. Pelle, P. Goldner, B. Bigot, A. Collet, Theoretical and experimental investigations of the nonlinear optical properties of vanillin. polyenovanillin, And bisvanillin derivatives, J Am Chem 116 (1994) 2094.
[56] V.M. Geskin, C. Lambert, J.L. Bredas, Origin of high second- and third-order nonlinear optical response in ammonio / boratodiphenylpolyene zwitterions: the remarkable role of polarized aromatic groups, J. Am. Chem. 125 (2003) 15651.
[57] N. Dege, N. Şenyüz, H. Batı, N. Günay, D. Avcı, Ö. Tamer, Y. Atalay, The synthesis. characterization and theoretical study on nicotinic acid [1-(2. 3-dihydroxyphenyl) methylidene] hydrazide , Spectrochim Acta A 120, (2014) 323.
[58] N. Öner, Ö. Tamer, D. Avcı, Y. Atalay, SpectrochimActa A 133 (2014) 542.
[59] R. Rahmani, N. Boukabcha, A. Chouaih, F. Hamzaoui, S. Goumri-Said, On the molecular structure, vibrational spectra, HOMO-LUMO, molecular electrostatic potential, UV-Vis, first order hyperpolarizability, and thermodynamic investigations of 3-(4-chlorophenyl)-1-(1yridine-3-yl) prop-2-en-1-one by quantum chemistry calculations, J. Mol. Struct. 1155 (2018) 484–495.
[60] D.A. Kleinman, Nonlinear dielectric polarization in optical media, Phys. Rev. 126 (1962) 1977–1979.
[61] S. Yahiaoui, A. Moliterni, N. Corriero, C. Cuocci, K. Toubal, A.Chouaih, A. Djafri, F. Hamzaoui, 2-thioxo- 3N-(2-methoxyphenyl) -5 [4'-methyl -3'N-(2'-methoxyphenyl) thiazol-2'(30H)-ylidene] thiazolidin-4-one:Synthesis. characterization. X-ray single crystal structure investigation and quantum chemical calculations, J. Mol. Struct. 1177, 186 (2019).
[62] L.T. Cheng, W. Tam, S.H. Stevenson, G.R. Meredith, G. Rikken, S.R. Marder, Experimental investigations of organic molecular nonlinear optical polarizabilities. 1. Methods and results on benzene and stilbene derivatives, J. Phys. Chem. 95 (1991) 1063.
[63] D. Jaya Reshmi, H. Marshan Robert, D. Aruldhas, I. Hubert Joe, S. Balachandran, Spectroscopic characterization and structural insights of 4,4,4-trifluoro-1-(2-naphthyl)-1,3-butanedione using vibrational, optical, electronic spectra, re duce d density gradient and quantum chemical calculations, J. Mol. Struct. 1231 (2021), 129675.
[64] J.S. Murray, K. Sen, Molecular electrostatic potentials: concepts and applications, Elsevier, 1996.
[65] G. Mahalakshmi, V. Balachandran, NBO.HOMO. LUMO analysis and vibrational spectra (FTIR and FT-Raman) of 1-Amino 4-methylpiperazine using ab initio HF and DFT methods, Spectrochim, ActaAMolBiomol.Spectrosc. 135 (2015) 321.
[66] N. Boukabcha, A. Feddag, R. Rahmani, A. Chouaih, F. Hamzaoui, Molecular structure, multipolar charge density study and nonlinear optical properties of 4-methyl-N-[(5-nitrothiophen-2-ylmethylidene)] aniline, J. Optoelectron. Adv. Mater. 20 (2018) 140.
[67] R. Zhang, B. Dub, G. Sun, Y. Sun, Experimental and theoretical studies on o-, m- and p-chlorobenzylideneaminoantipyrines, Spectrochim. Acta A 75 (2010) 1115.
[68] M.J. Turner, S.P. Thomas, M.W. Shi, D. Jayatilaka, M.A. Spackman, Chem. Commun. 51 (2015) 3735–3738.
[69] M.J. Turner, S. Grabowsky, D. Jayatilaka, M.A. Spackman, J. Phys. Chem. Lett. 5 (2014) 4249–4255.
[70] C.F. Mackenzie, P.R. Spackman, D. Jayatilaka, M.A. Spackman, IUCrJ 4 (2017) 575–587.